First-principles investigation of hydrogen interaction with TiC precipitates in α-Fe

Davide Di Stefano,[1,*] Roman Nazarov,[2,3] Tilmann Hickel,[2] Jörg Neugebauer,[2] Matous Mrovec,[1,4,†] and Christian Elsässer[1,5]

[1] *Fraunhofer-Institut für Werkstoffmechanik IWM, Wöhlerstr. 11, 79108 Freiburg, Germany*
[2] *Max-Planck-Institut für Eisenforschung GmbH, D-40237 Düsseldorf, Germany.*
[3] *Lawrence Livermore National Lab, Livermore, CA, USA*
[4] *Institut für Angewandte Materialien (IAM), Karlsruher Institut für Technologie, Engelbert-Arnold-Str. 4, 76131 Karlsruhe, Germany*
[5] *Albert-Ludwigs-Universität Freiburg, Freiburger Materialforschungszentrum (FMF), Stefan-Meier-Str. 21, 79104 Freiburg, Germany*

(Dated: May 7, 2016)

A correct description of hydrogen diffusion and trapping is the prerequisite for an understanding of the phenomenon of hydrogen embrittlement. In this study, we carried out extensive first-principles calculations based on density functional theory to investigate the interaction of H with TiC precipitates that are assumed to be efficient trapping agents mitigating HE in advanced high-strength steels. We found that there exists a large variety of possible trapping sites for H associated with different types of interfaces between the TiC particle and the Fe matrix, with misfit dislocations and other defects at these interfaces, and with carbon vacancies in TiC. The most efficient trapping by more than 1 eV occurs at carbon vacancies in the interior of TiC particles. However, these traps are difficult to populate at ambient temperatures since the energy barrier for H entering the particles is high. H trapping at the semicoherent interfaces between the TiC particles and the Fe matrix is moderate, ranging from 0.3 to 0.5 eV. However, a sufficiently large concentration of the carbide particles can significantly reduce the amount of H segregated at dislocation cores in the Fe matrix. A systematic comparison of the obtained theoretical results with available experimental observations reveals a consistent picture of hydrogen trapping at the TiC particles that is expected to be qualitatively valid also for other carbide precipitates with the rock-salt crystal structure.

I. INTRODUCTION

There has been a growing interest to expand the use of advanced high strength steels (AHSS) to a broader variety of structural applications. The ability of AHSS to withstand significantly higher stresses ($>$ 1 GPa) than ordinary steels enables to reduce the weight of structural components while maintaining the same stiffness and strength. Unfortunately, the susceptibility of steels to hydrogen embrittlement (HE) also increases with their strength and with the complexity of their microstructures[1–12].

In the case of AHSS, H-induced degradation can occur already at extremely low H concentrations of only a few ppm[8,10]. Since such low concentrations are practically unavoidable during production and service, one possible strategy to improve the resistance of AHSS to HE is to render H innocuous by introducing a sufficient amount of effective traps (e.g., lattice defects, solute atoms, secondary-phase particles) in the microstructure of the material[13,14]. These traps can significantly lower the chemical potential and the overall amount of diffusible H, provided that the H supply from the environment is suppressed (e.g., by a protective surface coating). Furthermore, an efficient trapping leads to a reduction of the effective diffusivity of H in the material. Both effects may delay the formation of microcracks as well as their propagation since the critical H levels cannot be reached or maintained.

It has been reported in a number of experimental studies[13–27] that steels with uniform distributions of fine carbide and nitride precipitates indeed have a lower susceptibility to HE. The improved resistance is assumed to be due to new trapping sites inside the precipitates or at the interfaces between the precipitates and the steel matrix. However, there are still open questions regarding the exact microscopic nature of these trapping sites and their effectiveness in immobilizing H. To answer these questions experimentally is a rather difficult task because the most common techniques applied for investigations of H trapping, such as thermal desorption spectroscopy[20,22,24,26,28] or electrochemical permeation measurements[13,28,29], provide only indirect information whose analysis and interpretation is not always straightforward[24,28–30]. Consequently, a broad range of binding and detrapping energies has been reported in the literature.

A possible explanation for these large variations can be related to a different trapping behavior of particles with different sizes, morphologies, and interface characters (coherent, semicoherent, or incoherent)[22]. Recently, Takahashi et al.[23,31] carried out first direct observations of hydrogen isotopes at VC and TiC particles using atom probe tomography. These studies revealed that most H atoms are located on the extended basal interfaces of platelet-like precipitates and that larger particles trap H more effectively than smaller ones. Based on these observations, it was speculated that either misfit dislocations or carbon vacancies at the interfaces are the most favorable trapping sites, but no direct evidence could be

provided.

Atomistic simulations can help to resolve these uncertainties and to gain insight into microscopic mechanisms of hydrogen diffusion and trapping. Nowadays, the most reliable means for theoretical studies of materials properties at the atomic scale are first-principles calculations based on density functional theory (DFT) that can be applied to virtually every material. Binding and activation energies of hydrogen within the bulk matrix or the precipitate can be determined relatively easily using DFT, without the need of additional assumptions or simplifications[32,33]. To accurately capture the interaction of H with the simplest imperfections of crystals, such as atomic vacancies[34–36] or symmetric tilt or twist grain boundaries[37,38], is a more challenging but still doable task for DFT computations. Investigating the impact of precipitates, however, requires a careful consideration of interfaces between two different crystal structures that are not perfectly matching. In these cases, it is essential to develop efficient yet reliable strategies to predict H trapping for various interface configurations, including not only coherent but also semi- and incoherent boundaries as well as interfaces containing additional atomic point defects.

In the present paper, we provide such a strategy as part of an extensive and systematic DFT study of interactions of H with various microstructural features associated with TiC precipitates in body-centered cubic (bcc) α-Fe. We first investigate how H interacts with both individual phases and with point defects embedded in their bulk interiors. In the next step, we study H segregation at various interface configurations, which are defect-free or contain carbon vacancies. At last, we combine the results to obtain segregation, escape and migration energies that can be related to different microstructural features associated with TiC precipitates. Our analysis reveals that there is no single trapping energy characteristic for all TiC particles, but the trapping depends sensitively on the particle size, stoichiometry, morphology, and the nature of the particle-matrix interface. In this way, we provide an explanation of the variety of experimental results that exist in the literature.

II. THEORETICAL APPROACH

A system consisting of a transition-metal carbide particle in the matrix of bcc Fe is rather complicated to model. Both morphology and size of transition-metal carbides precipitated in steels can vary significantly depending on composition and manufacturing conditions (e.g., thermal treatment)[20–22,39–41]. Furthermore, the carbides are often sub-stoichiometric, containing a large amount of C vacancies. Because of this complexity, simulations of the whole particle at the atomic scale are infeasible with electronic structure methods. To overcome this problem we therefore considered independently the interaction of H with bulk TiC (both perfect and with C vacancies) and with various representative interfaces between TiC particle and Fe matrix.

Small TiC nuclei are expected to be fully coherent with the bcc Fe matrix[20]. The preferential growth occurs along the {100} planes of bcc Fe[20] and the particles adopt the so-called Baker-Nutting (B-N) orientation relationship (OR) with $(001)_{\mathrm{Fe}}||(001)_{\mathrm{TiC}}$ and $[100]_{\mathrm{Fe}}||[110]_{\mathrm{TiC}}$. As the precipitates grow, they take a typical shape of thin platelets where misfit dislocations form on the broad $(001)_{\mathrm{Fe}}/(001)_{\mathrm{TiC}}$ interface when the particle diameter exceeds about 4 nm[20,22]. The lateral interfaces are often round with a tendency to facet along the $\{100\}_{\mathrm{Fe}}$ and $\{110\}_{\mathrm{Fe}}$ planes. Larger particles become ellipsoidal and form less coherent interfaces due to deviations from the exact B-N OR. A detailed experimental analysis of TiC precipitates in steels can be found in the papers of Wei et al.[20,22] and references therein.

For our atomistic simulations, the coherent interfaces are the simplest ones to model. They are characterized by a perfect coincidence of atomic planes across the interface, where the eventual lattice mismatch is accommodated by elastic expansion/compression of one or both phases. These systems can be therefore represented by relatively small, periodically repeated supercell models (see below).

In the case of semicoherent interfaces, the elastic energy needed to make the interface coherent becomes prohibitively large and it is more favorable to form an array of misfit dislocations to release the accumulated elastic stress. The spacing between the misfit dislocations, which generally depends on the lattice mismatch and elastic properties of the two materials, is typically of the order of several nanometers. This clearly increases enormously the computational costs, since a full model of such a semicoherent interface requires thousands of atoms[42,43]. Fortunately, the semicoherent interface can be well approximated as being composed of broad coherent regions that are periodically interrupted by relative narrow regions containing the misfit dislocation cores[42,44], as shown schematically in Fig. 1. The atomic structure of a misfit dislocation core can again be represented using a small supercell, in which the two crystals in contact are laterally translated with respect to each other. In this case, the long range elastic strain field of the dislocation is neglected.

In the case of general interfaces[45], here also referred to as incoherent interfaces, i.e., interfaces with more distorted atomic structures that lack a well-defined periodicity, the variability of possible supercell models is large. In this work, we investigated the $(110)_{\mathrm{Fe}}/(001)_{\mathrm{TiC}}$ interface as well as several defective interfaces (containing C vacancies) as representative models for general (incoherent) interfaces. A detailed description of these interfaces is given in the next sections.

To characterize the stability of an interface, it is pos-

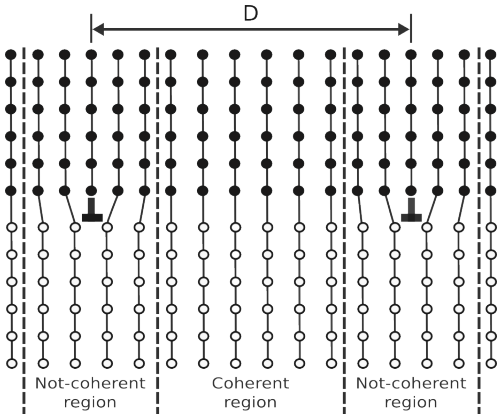

FIG. 1. Schematic representation of the semicoherent interface

sible to calculate the interface energy defined as:

$$\gamma_{\rm int} = \left[E_{\rm tot}(Fe_x/Ti_yC_y) - E_{\rm tot}(Fe_x^{\rm bulk}) - E_{\rm tot}(Ti_yC_y^{\rm bulk})\right]/2A \quad (1)$$

where $E_{\rm tot}(Fe_x/Ti_yC_y)$ is the total energy of supercell containing the investigated interface configuration, while $E_{\rm tot}(Fe_x^{bulk})$ and $E_{\rm tot}(Ti_yC_y^{bulk})$ are the total energies of supercells containing the two bulk phases with the same numbers of atoms as in the interface supercell; A is the interfacial area, and the factor 2 in the denominator takes into account that there are two equal interfaces in the supercell.

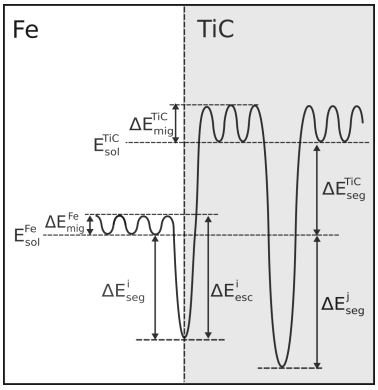

FIG. 2. Schematic diagram of energy profile associated with H trapping at a Fe/TiC interfaces and in the interior of an TiC precipitate containing a vacancy.

To characterize the energetics associated with H trapping, we adopt a nomenclature displayed in Fig. 2. The solution energy of an isolated interstitial H atom inside perfect bulk Fe or TiC crystals are defined as

$$E_{sol}^{bulk} = E_{\rm tot}^{bulk}(H) - E_{\rm tot}^{bulk} - \frac{1}{2}E[H_{2(g)}], \quad (2)$$

where $E_{\rm tot}^{bulk}(H)$ and $E_{\rm tot}^{bulk}$ are the total energies of the bulk supercells with and without H, respectively, and $E[H_{2(g)}]$ is the total energy of the hydrogen molecule. As will be explained later, we consider the solution energy of H in bcc Fe, $E_{sol}^{\rm Fe}$, to be the reference state for the analysis of H segregation at the interfaces.

The segregation energy of H in a trap i is then given as:

$$\Delta E_{\rm seg}^i = E_{\rm tot}^i(H) - E_{\rm tot}^i(0) - \left[E_{\rm tot}^{Fe_{\rm bulk}}(H) - E_{\rm tot}^{Fe_{\rm bulk}}(0)\right] \quad (3)$$

where $E_{\rm tot}^i(H)$ and $E_{\rm tot}^i(0)$ are the total energies of the system containing the trap i with and without H, respectively, while $E_{\rm tot}^{Fe_{\rm bulk}}(H)$ and $E_{\rm tot}^{Fe_{\rm bulk}}(0)$ are the total energies of a bulk Fe crystal supercell with and without H, respectively. Using this definition, negative values of $\Delta E_{\rm seg}^i$ indicate that the considered site is energetically more favorable for H than the tetrahedral interstitial site in bulk bcc Fe. The energy barriers for H migration in Fe and TiC, $\Delta E_{\rm mig}^{\rm Fe}$ and $\Delta E_{\rm mig}^{\rm TiC}$, respectively, are considered to be equal to their bulk values, unless noted otherwise (see below).

We define a trap escape energy, which is the energy needed for H to escape from a trap i to bulk Fe, either as

$$\Delta E_{\rm esc}^i = \Delta E_{\rm seg}^i + \Delta E_{\rm mig}^{\rm Fe} \quad (4)$$

if H is trapped at the Fe/TiC interface, or as

$$\Delta E_{\rm esc}^i = \Delta E_{\rm seg}^i + \Delta E_{\rm seg}^{\rm TiC} + \Delta E_{\rm mig}^{\rm TiC} \quad (5)$$

if the considered trap is in the interior of the carbide.

III. COMPUTATIONAL DETAILS

All DFT calculations were carried out using the Vienna Ab-initio Simulation Package (VASP)[46–48]. The generalized gradient approximation (GGA) as given by Perdew, Burke and Ernzerhof[49] was employed for exchange-correlation. Ultrasoft pseudopotentials[50] were used for the core-valence interactions. We also performed a number of calculations with projector-augmented wave (PAW) potentials, but the results were found to be fully consistent with those obtained using the ultrasoft pseudopotentials. All calculations were carried out as spin-polarized. An energy cutoff of 300 eV for the plane-wave basis was found to yield converged total energies within an accuracy of 10^{-5} eV. The Brillouin zone was sampled using Monkhorst-Pack grids with various k-point densities (see below). Atom positions were relaxed until the residual forces acting on the atoms were less than 10^{-3} eV/Å and the total energy was converged to 10^{-5} eV. An inclusion of quantum mechanical effects is crucial for a correct description of H diffusion in bcc Fe[33,51,52], but in the case of H trapping, these effects should not affect significantly the escape rate of H from a trap. The energy path to escape a trap is typically asymmetric (e.g., qualitatively similar to that for H migration in fcc Ni),

so that quantum-mechanical effects are not critical, as shown in Ref. 33. All migration barriers calculated here correspond to transition-state configurations that are either symmetry-dictated extrema or saddle points whose energies can be obtained using a standard structural relaxation.

IV. RESULTS

A. Bulk phases

The fundamental properties of the individual bulk phases are summarized in Table I. The most stable interstitial sites for dilute hydrogen in bcc iron are the tetrahedral sites (T-sites)[53–55]. The obtained solution energy (cf. Eq. 2) of H in a 2x2x2 Fe supercell $Fe_{16}H$ is E_{sol}^{Fe} =0.16 eV, which agrees well with results of previous calculations[54,56].

As mentioned above, the chemical potential of H in bulk bcc Fe presents the most natural choice for a rigorous comparison of the segregation energies at the investigated microstructural features. We therefore use this quantity as a reference level for all calculations of H interactions with interfaces and other defects.

The classical migration barrier for H in bcc Fe has been calculated in Ref. 33 to be $\Delta E_{\rm mig}^{\rm Fe}$ =0.09 eV. This value also agrees well with the results of other theoretical studies[51–54].

	a	B	C_{11}	C_{12}	C_{44}	E_{sol}	$\Delta E_{\rm mig}$
Fe	2.856	175	258	133	94	0.16	0.09
TiC	4.338	248	508	118	168	0.84	0.29,0.47

TABLE I. Fundamental properties of the bulk phases: lattice parameter a in Å, elastic constants in GPa (taken from Ref.[39]), and solution and migration energies in eV. Note that the reported migration energy for H in bcc Fe is the classical one, and the two values for TiC correspond to two migration pathways shown in Fig. 3 (see text for a detailed description).

TiC crystallizes in the cubic NaCl structure which can be seen as an fcc Ti sublattice where every interstitial octahedral site is occupied by an C atom. We found that in perfect stoichiometric TiC the most stable positions for H atoms are not in the "cubic" interstitial sites, i.e., in the center of a cube whose corners are occupied by four Ti and four C atoms in alternating way (these are actually the tetrahedral sites of the fcc Ti and C sublattices), but in "trigonal" sites where the H atom is surrounded by three Ti atoms lying in a {111} plane. These interstitial sites together with transition states identified in our calculations are shown in Fig. 3. The 3D arrangement of the trigonal sites in TiC can be viewed as a lattice composed of regular tetrahedra whose corners always point to the C atoms. The migration of H between the neighboring trigonal sites can proceed either via long jumps within a single tetrahedron (e.g., the jump between the T_1 and T_2 sites in Fig. 3) or via short jumps between the neighboring tetrahedra (e.g., the jumps between the T_2 and T_3 sites or between the T_2 and T_4 sites in Fig. 3).

The solution energy for H in the trigonal sites, calculated for a 2x2x2 cubic TiC supercell ($Ti_{32}C_{32}$), amounts to $E_{sol}^{\rm TiC}$ =0.84 eV. This value is lower than that of 0.97 eV obtained by Ding et al.[57], but it is not clear which configuration the authors obtained.

According to our calculations, the lowest migration barrier of 0.29 eV is associated with the short T_2 to T_3 jump, corresponding to the saddle point S_3. The migration within the tetrahedron is more difficult and does not take place along the edge of the tetrahedron but via its center (the cubic site). The migration barrier for this transition, corresponding to the transition state S_1, amounts to 0.47 eV. An even higher migration barrier of 0.64 eV exists for the indirect jump T_2 to T_3 between the neighboring tetrahedra over the saddle point S_2. Since global percolation of H through the TiC crystal requires H to cross both saddle points S_1 and S_3, the governing migration barrier for H diffusion in bulk TiC is the higher barrier of 0.47 eV. Therefore, this value has been chosen as the characteristic barrier for the migration of H in bulk TiC.

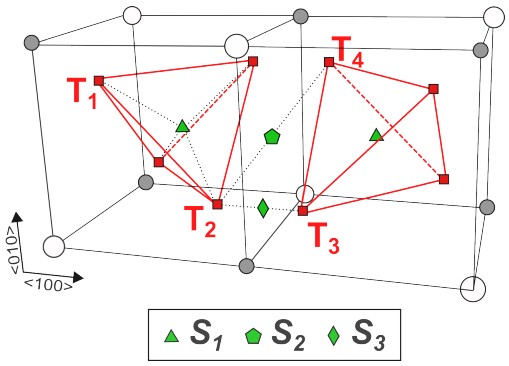

FIG. 3. Atomic structure of bulk TiC (Ti: white spheres, C: grey spheres) with marked trigonal (T) and saddle point (S_{1-3}) sites.

B. Coherent and semi-coherent interfaces

Based on experimental observations[20,21], we focused primarily on the Baker-Nutting OR, $(001)_{\rm Fe}/(001)_{\rm TiC}$ & $[100]_{\rm Fe}||[110]_{\rm TiC}$, for our calculations of the coherent and semi-coherent interfaces between bcc Fe and TiC phases. The lattice mismatch for this OR (cf. Table I) is accommodated by setting the initial lateral cell vectors of the used supercell to those of a unit cell of TiC, which is the stiffer phase (cf. Table I). Even when the mutual orientation of the two crystals is fixed, there are still additional geometrical degrees of freedom left, namely, the relative translations of the two crystals parallel and perpendicular to the interface plane.

We investigated three highly symmetric translation states, illustrated in Fig. 4, that we designate as (i) 'Fe-on-C' configuration, where the Fe atoms are on top of C atoms; (ii) 'Fe-on-Ti' configuration, where the Fe atoms are on top of Ti atoms; and (iii) 'Bridge' configuration, where the Fe atoms have two C atoms and two Ti atoms as nearest neighbors.

For the calculations of perfect interfaces, we employed supercells composed of 5 Fe layers, each containing one Fe atom, and 5 layers of TiC, each containing one C atom and one Ti atom. For this supercell a 10x10x2 k-point mesh was used for the Brillouin-zone integration. The supercells obtained after complete relaxation (cell vectors and atomic positions) are shown in Fig. 5 and their optimized geometrical parameters are summarized in Table II.

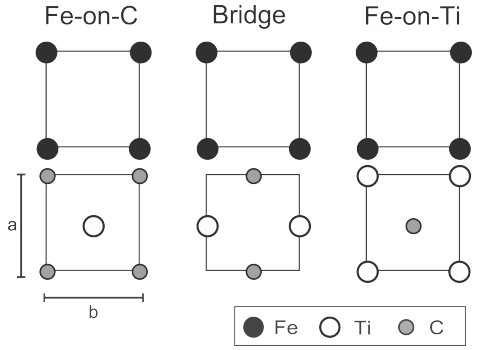

FIG. 4. A schematic representation of three investigated translation states for the $(001)_{\mathrm{Fe}}/(001)_{\mathrm{TiC}}$ interface obtained by different relative shifts of the two crystals. Top and bottom panels represent the $(001)_{\mathrm{Fe}}$ and the $(001)_{\mathrm{TiC}}$ interface planes, respectively.

	a	b	c	$d_{\mathrm{Fe\text{-}C}}$	$d_{\mathrm{Fe\text{-}Ti}}$	γ_{int}
Fe-on-C	3.04	3.04	17.81	1.91	1.98	0.06
bridge	3.10	2.97	17.85	1.65	2.00	0.25
Fe-on-Ti	3.01	3.01	19.69	2.72	2.88	0.48

TABLE II. Supercell dimensions a, b and c, and the interface spacing d_{Fe-Ti} corresponding to the distance between the interfacial Fe and Ti atoms along the $\langle 001\rangle$ direction (all values are in Å). The interface energy, γ_{int}, for the three investigated $(001)_{\mathrm{Fe}}/(001)_{\mathrm{TiC}}$ configurations is given in eV/Å^2.

In all three cases, the lattice vectors parallel to the interface are close to that of bulk TiC (3.06 Å). This confirms that the bi-axial stress due to the lattice mismatch is mainly accommodated by stretching of the Fe matrix (by about 6.6%). This result is consistent with the larger elastic stiffness of TiC compared to α-Fe (cf. Table I). The lattice mismatch can be used to estimate[58] the distance, $D = 4.6$ nm, between two misfit dislocations (see Fig. 1) that also corresponds to the maximum size of a coherent TiC precipitate.

The calculated interface energies, shown in Table II, indicate that the most stable interface is the Fe-on-C

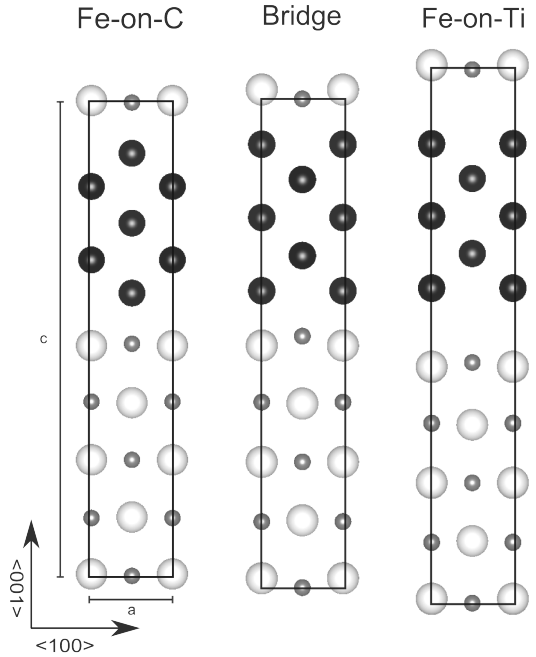

FIG. 5. Atomic structures of the three investigated configurations of the $(001)_{\mathrm{Fe}}/(001)_{\mathrm{TiC}}$ interface (see Fig. 4) after a complete relaxation of all degrees of freedom. Black, grey, and white spheres represent Fe, C, and Ti atoms, respectively.

configuration, followed by the Bridge and Fe-on-Ti configurations. Therefore, the coherent part of the Fe/TiC interface will most likely correspond to the Fe-on-C configuration. The other two configurations can be related to dislocation cores and their intersections that appear on the semicoherent interface. The misfit dislocation cores at this interface consist essentially of an extra Fe plane[22]. As a result, the Fe bicrystal is in the core center shifted with respect to TiC by a half inter-planar spacing along either the $\langle 110\rangle_{\mathrm{Fe}}$ or $\langle \bar{1}10\rangle_{\mathrm{Fe}}$ directions. Both these translations result in the Bridge configuration which thus resembles the misfit dislocation core. When two perpendicular misfit dislocations along $\langle 110\rangle_{\mathrm{Fe}}$ and $\langle \bar{1}10\rangle_{\mathrm{Fe}}$ intersect, the total displacement of the two crystals results in the Fe-on-Ti configuration at the intersection of the dislocation cores.

C. Other interfaces

According to experimental studies[20–22], the TiC particles in the Fe matrix can form also interfaces with other ORs, in particular those with $(110)_{\mathrm{Fe}}/(001)_{\mathrm{TiC}}$ orientation. In this case, it is more difficult to find a geometrically favorable orientation of the two crystals with a small lattice mismatch. We chose the configuration shown in Fig. 6.

This interface was obtained by joining three unit cells of bcc Fe with two unit cells of TiC. This construction allows for a very small mismatch along the $\langle 001\rangle_{\mathrm{Fe}}$

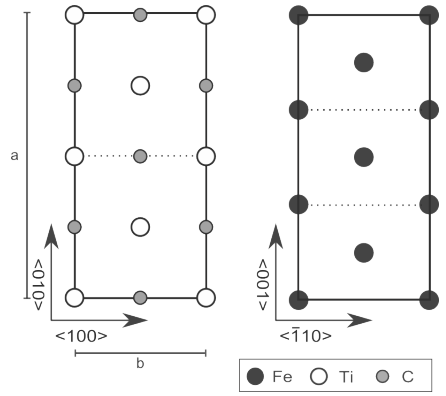

FIG. 6. Schematic representation of the two adjoining Fe and TiC planes across the $(011)_{\mathrm{Fe}}/(001)_{\mathrm{TiC}}$ interface. Black, grey, and white spheres represent Fe, C, and Ti atoms, respectively.

($\langle 010\rangle_{\mathrm{TiC}}$) direction of only about 2%, and still an acceptable mismatch of about 8% along the $\langle 1\bar{1}0\rangle_{\mathrm{Fe}}$ ($\langle 100\rangle_{\mathrm{TiC}}$) direction. Note that in this case the relative shift of the two crystals with respect to each other by $1/2\langle 001\rangle_{\mathrm{Fe}}$ does not change the interface structure. This interface cannot be considered as coherent because the patterns of atoms at the adjoining planes are very different (cf. Fig. 6) and a good match between the two crystals is not possible.

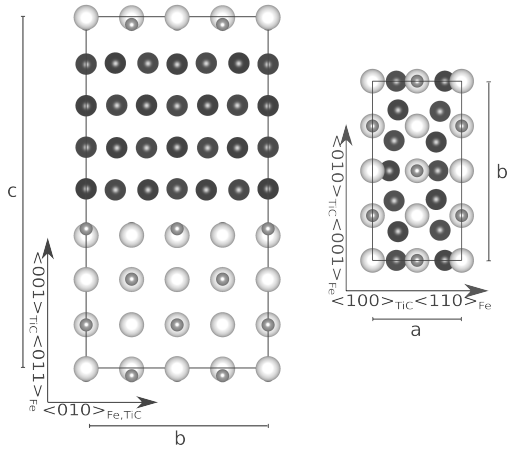

FIG. 7. Atomic structure of the $(011)_{\mathrm{Fe}}/(001)_{\mathrm{TiC}}$ supercell after a complete relaxation of all degrees of freedom. Black, grey, and white sphere represent Fe, C, and Ti atoms, respectively.

Our supercell used to model this interface consisted of four Fe planes, each containing 6 Fe atoms, and 4 TiC planes, each containing 4 Ti and 4 C atoms. The Brillouin zone integration was done on a 10x5x2 k-point mesh. As in the case of the $(001)_{\mathrm{Fe}}/(001)_{\mathrm{TiC}}$ supercells, we performed a full relaxation of all degrees of freedom. The obtained relaxed structure is shown in Fig. 7, and the supercell dimensions and the interface energy are listed in Table III. From Fig. 7 one can see that the poor match between the two crystals results in a large atomic distortion within the interfacial planes. Similarly as for the interfaces considered in the previous section, the lattice mismatch between the two crystal structures is mainly accommodated by an expansion of the Fe crystal only.

a	b	c	$d_{\mathrm{Fe\text{-}C}}$	$d_{\mathrm{Fe\text{-}Ti}}$	γ_{int}
4.28	8.59	16.56	1.82	2.15	0.15

TABLE III. Supercell dimensions, interplanar distances along the $\langle 100\rangle$ direction between the Fe and C planes, and the Fe an Ti planes across the interface (in distances are in Å), and the interface energy (in eV/Å^2) for the investigated $(011)_{\mathrm{Fe}}/(001)_{\mathrm{TiC}}$ interface.

D. Trapping of H at interfaces

$(001)_{Fe}/(001)_{TiC}$ interfaces

For all the three possible interface configurations (Fe-on-C, Bridge, and Fe-on-Ti) described in Sec. IV B, we identified and characterized a number of possible trap sites for H. These sites were found by placing an H atom at different high-symmetry positions at the interface and at octahedral-like and tetrahedral-like sites in the Fe plane closest to the interface, and optimizing the atomic positions. This procedure allowed us to sample various atomic configurations and to identify the stable sites for H.

Most of the calculations were carried out using the same interface supercells described above (see Fig. 5). However, we carried out extensive validation calculations with larger supercells extended both along and perpendicular to the interface to test whether the supercell size is sufficient for a reliable description of the H segregation. These test calculations, described in detail in the Appendix A, showed that all employed supercell models are sufficiently large to avoid any serious finite-size effects on the computed segregation energies.

The energetically most stable sites for H at the Fe-on-C, Bridge, and Fe-on-Ti configurations obtained in our calculations are shown in Fig. 8. Surprisingly, most of them are not located in the interface region between the two crystals but at the Fe plane closest to the interface (these sites are marked with green symbols). Only for the least stable Fe-on-Ti configuration, there exist also two meta-stable sites (marked by blue and red symbols) in the interface region. Note that most of the stable sites have similar symmetries as octahedral and tetrahedral sites in bulk Fe. For instance, in the Fe-on-C configuration the sites marked with a triangle resemble tetrahedral sites where one vertex of the Fe tetrahedron is replaced with an Ti atom. Similarly, the sites marked with squares, pentagons and diamonds have a similar symmetry as the octahedral sites in bulk bcc Fe.

To distinguish between the various sites, we designate the sites at the Fe plane and in the interface region using

labels FP_x^y and IP_x^y, respectively. The subscript x marks the specific site index while the superscript y indicates the type of the interface configuration ("A" for Fe-on-C, "B" for Bridge, and "C" for Fe-on-Ti).

Fe-on-C (A)		Bridge (B)		Fe-on-Ti (C)	
Site	$\Delta E_{\rm seg}$	Site	$\Delta E_{\rm seg}$	Site	$\Delta E_{\rm seg}$
FP_1^A	−0.30	FP_1^B	−0.23	FP_1^C	−0.50
FP_2^A	−0.16	FP_2^B	−0.20	IP_1^C	−0.42
FP_3^A	−0.32	FP_3^B	−0.08	IP_2^C	−0.40
		FP_4^B	−0.49		

TABLE IV. Calculated segregation energies (in eV) for different stable positions for H at the $(001)_{\rm Fe}/(001)_{\rm TiC}$ interface. The labels for the sites refer to the positions illustrated in Fig. 8

The segregation energies for H, calculated according to Eq. 3, are reported in Table IV. For the Fe-on-C configuration, the most stable positions for H are in the tetrahedral-like sites FP_3^A (triangles) and the octahedral-like sites FP_1^A (squares) with almost identical segregation energies of about −0.3 eV. The octahedral-like sites FP_2^A (pentagons) in the middle of the Fe plane are the least stable ones.

For the Bridge configuration, the most favorable sites for H are again the tetrahedral-like sites FP_4^B with the segregation energy of almost −0.5 eV. All the remaining sites are significantly less favorable.

The Fe-on-Ti configuration is the only one where H segregates not only at the Fe plane but also in the interface region in between the two materials. The absolute segregation energies for all identified sites are relatively large, ranging between −0.5 and −0.4 eV.

To analyze the influence of the dilation of the Fe lattice in the vicinity of the coherent interface, we also computed the segregation energy for an H atom at the tetrahedral position in bulk Fe that was elastically strained in the same way as in the interface supercell. We found that the segregation energy at such dilated Fe bulk lattice amounts to −0.18 eV. By comparing this value with the segregation energies in Table IV it is possible to conclude that the favorable trapping is due to both the elastic straining of the Fe lattice and the chemical environment at the interface. However, the chemical effects prevail for the interface configurations mimicking the misfit dislocation cores (i.e., Bridge and Fe-on-Ti).

$(011)_{Fe}/(001)_{TiC}$ *interface*

In the case of the $(011)_{\rm Fe}/(001)_{\rm TiC}$ interface, to locate the stable positions for H atoms by symmetry is not a straightforward task because the interface is rather distorted and does not have any high-symmetry interstitial sites. We therefore created several initial configurations with an H atom placed at different, randomly chosen initial positions at the interface plane and relaxed these configurations. In this way, three stable positions for H have been identified. Similarly to the $(001)_{\rm Fe}/(001)_{\rm TiC}$ interface configurations, we found that H prefers not to reside in the interface region but rather to move into Fe. One of the relaxed structures (others are qualitatively similar) showing the position of H in the Fe plane adjacent to the interface is displayed in Fig. 9. The computed segregation energies for all stable sites are between −0.20 and −0.10 eV.

As for the $(001)_{\rm Fe}/(001)_{\rm TiC}$ interface, we also calculated the segregation energy for bulk Fe strained as in the interface supercell. The obtained value of −0.14 eV indicates that the trapping effect at the $(011)_{\rm Fe}/(001)_{\rm TiC}$ is mainly due to the straining of the Fe lattice.

E. Interaction of H with C vacancies

Apart from the perfect interfaces, we calculated the trapping properties of C vacancies, both at the two interfaces and in the interior of the carbide. Transition-metal carbides including TiC are known to exhibit large stoichiometric variations of the carbon sublattice, with the amount of C vacancies reaching up to 50%[59–63]. Since the migration energy of a C vacancy is very high (our calculated value is about 4 eV), the vacancies are essentially immobile. Nevertheless, such a high substoichiometry may lead to a continuous network of interconnected vacancies[60,61], from the interface to the interior of the precipitate, that can facilitate H diffusion and trapping (see Sec. V.B).

In all investigated cases, the most stable site for H is in the center of the C vacancy. This result is consistent with experimental observations[64]. For the $(001)_{\rm Fe}/(001)_{\rm TiC}$ interface, only the most stable Fe-on-C interface configuration was considered. We investigated three distinct vacancy locations (V_1, V_2 and V_3) at different distances from the interface, as illustrated in Fig. 10. For these calculations, we kept the supercell dimension in the direction perpendicular to the interface but doubled the lateral dimensions parallel to the interface (i.e., the supercell was quadrupled in size) in order to reduce the interactions between periodic images of the C vacancies and the H atoms.

For the $(011)_{\rm Fe}/(001)_{\rm TiC}$ interface, we considered just one configuration with the vacancy (labeled as V_4) located in the TiC layer directly at the interface. Since the supercell used for this interface was sufficiently large, it was not further extended for the vacancy calculations.

For both interfaces, the calculated H segregation energies, $\Delta E_{\rm seg}^{vac}$, are listed in Table V. For comparison, we report also the results obtained for a C vacancy in bulk TiC crystal, $V_{\rm TiC}^{\rm H}$, calculated for a $Ti_{32}C_{31}$ supercell. In this case, we also calculated the segregation energy for a double H occupation, $V_{\rm TiC}^{\rm 2H}$. In addition to the segregation energies, we computed also the energy barrier for H migration between two neighboring vacancies in bulk

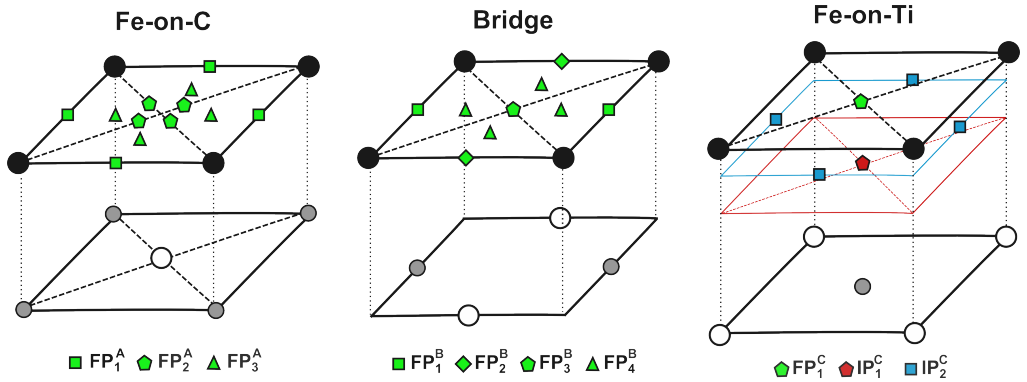

FIG. 8. (Color online) Schematic representation of the stable positions for H at the Fe-on-Ti, Bridge, and Fe-on-Ti configurations of the $(001)_{\mathrm{Fe}}/(001)_{\mathrm{TiC}}$ interface. The black, grey, and white circles represent Fe, C, and Ti atoms, respectively. Only one Fe and one TiC planes directly adjacent to the interface are displayed.

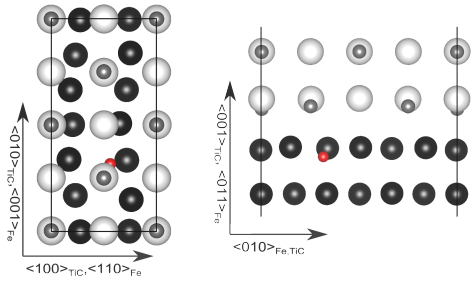

FIG. 9. (color online) A representative example of H (red sphere) segregated at the $(110)_{\mathrm{Fe}}/(001)_{\mathrm{TiC}}$ interface. In the left panel, only the Fe and TiC interfacial planes are shown.

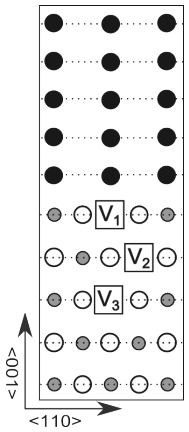

FIG. 10. Illustration of the different C vacancies positions considered in the vicinity of the $(001)_{\mathrm{Fe}}/(001)_{\mathrm{TiC}}$ coherent interface.

TiC. Our obtained value of 1.19 eV is the same as that reported by Ding et al.[57].

F. Summary of characteristic segregation energies

As the number and variability of the obtained results is large, we summarize the key quantities and their relation to specific microstructural features in Table VI. Here we assumed that the characteristic segregation energy for each trap source is that of the deepest trap site, i.e., that at reasonable H concentrations only the deepest traps will be occupied. The data in this Table serve as a basis for combining the theoretical predictions with experimental observation into a consistent picture of H segregation at TiC particles.

Bulk TiC		$(001)_{\mathrm{Fe}}/(001)_{\mathrm{TiC}}$			$(011)_{\mathrm{Fe}}/(001)_{\mathrm{TiC}}$
V_{TiC}^{H}	V_{TiC}^{2H}	V_1	V_2	V_3	V_4
−1.09	−0.07	−0.46	−0.86	−0.88	−0.90

TABLE V. Segregation energies for an H atom at C vacancies in bulk TiC (for single and double H occupancy) and at the $(001)_{\mathrm{Fe}}/(001)_{\mathrm{TiC}}$ and $(110)_{\mathrm{Fe}}/(001)_{\mathrm{TiC}}$ interfaces (all values are in eV).

Trapping feature	Label	ΔE_{seg} [eV]
$(001)_{\mathrm{Fe}}/(001)_{\mathrm{TiC}}$ interface		
Broad coherent interface	$(001)_{\mathrm{int}}$	−0.32
Dislocation core	disl-cores[a]	−0.49
Dislocation intersection		−0.50
C vacancy	V-$(001)_{\mathrm{int}}$	−0.46
$(110)_{\mathrm{Fe}}/(001)_{\mathrm{TiC}}$ interface		
Incoherent interface	$(110)_{\mathrm{int}}$	−0.20
C vacancy	V-$(110)_{\mathrm{int}}$	−0.90
Bulk TiC		
C vacancy with one H	V_{TiC}^{H}	−1.09
C vacancy with two H	V_{TiC}^{2H}	−0.07

[a] Since the segregation energy is almost the same, we further consider the dislocation cores and their intersections as a single trap site.

TABLE VI. Characteristic segregation energies of the investigated traps sources.

V. DISCUSSION

A. Interface structures

For the $(001)_{\mathrm{Fe}}/(001)_{\mathrm{TiC}}$ interface, three different configurations (see Figs. 4 and 5) were investigated. In all cases, the lattice mismatch between the two crystals is primarily accommodated by a lateral elastic expansion of the Fe crystal (6.6%) in agreement with previous studies by Fors and Wahnström[39] and Kawakami and Matsumiya[65]. From the lattice mismatch between the Fe and TiC at coherent interface, we calculated[58] the maximum size of a fully coherent precipitate to be 4.6 nm. This value corresponds also to the distance between the misfit dislocation in the semi-coherent interface, and agrees well with the experimental value of 4.2 nm reported by Wei and Tsuzaki[22].

The analysis of the interface energies (Table II) reveals that the Fe-on-C configuration is the most stable one. As shown by Fors and Wahnström[39], this is primarily due to strong chemical bonds between Fe and C atoms that are similar to those between Ti and C atoms. Therefore, the interfacial Fe layer acts as a natural extension of the TiC phase. This is not the case for the other two interfaces and hence they are less stable.

Due to its stability, the Fe-on-C configuration will likely be the predominant interface type between the Fe matrix and the smallest cuboidal coherent TiC particles, and it will constitute the broad, coherent interface regions of the larger semi-coherent TiC platelets. The Bridge and the Fe-on-Ti configurations correspond approximately to atomic arrangements at the misfit dislocation core and at the intersection of two perpendicular misfit dislocation cores at the $(001)_{\mathrm{Fe}}/(001)_{\mathrm{TiC}}$ interfaces, respectively. By combining our results for these different configurations, it is possible to device an overall picture of the trapping behavior of H atoms at the $(001)_{\mathrm{Fe}}/(001)_{\mathrm{TiC}}$ semi-coherent interfaces. This requires three main approximations: (i) the semi-coherent interface is considered to be composed of wide sections of a fully coherent interface periodically interrupted by narrow misfit dislocation cores, as illustrated in Fig. 1; (ii) both regions can be treated separately; and (iii) the long-range strain field of the misfit dislocations is neglected and only the dislocation cores and their intersections are considered. The validity of these approximations has been examined in several studies[42–44,66,67]. Recent direct comparison of Sawada et al.[43] confirmed that the atomic structure and properties of the Fe/NbC semi-coherent interface modeled at a full scale (large system with explicit misfit dislocations) indeed closely resemble approximate structural models employed in this work.

Interfaces with the $(011)_{\mathrm{Fe}}/(001)_{\mathrm{TiC}}$ orientation, were investigated as well. Experimental investigations[22] report that the lateral incoherent sides of the disk-shaped TiC precipitates tend to facet towards the $(011)_{\mathrm{Fe}}/(001)_{\mathrm{TiC}}$ orientation. Due to a poor lattice matching between bcc Fe and TiC for this orientation relationship (cf. Fig. 6), the atomic structure of this interface is likely to be highly distorted, without a clear pattern of coherent regions separated by misfit dislocations as in the $(001)_{\mathrm{Fe}}/(001)_{\mathrm{TiC}}$ semi-coherent interface. Nevertheless, the obtained interface energy (cf. Table III) is similar to that of the coherent interface, indicating that the $(011)_{\mathrm{Fe}}/(001)_{\mathrm{TiC}}$ interface is rather stable and therefore likely to be observed in experimental studies. The good stability of the interface is again probably related to strong chemical bonds formed between Fe and C atoms across the interface. Similar conclusions were obtained for this interface by Arya and Carter[68].

B. Interaction of H with TiC precipitates in Fe

In order to characterize the H trapping properties of TiC precipitates in Fe, we considered both the interfaces and the interior of the precipitate. For each considered case, we obtained a large variety of possible traps. Based on the obtained results, it is possible to construct energy profiles experienced by H atoms around the different types of interfaces (see Fig. 11). Note that for each investigated case we assumed that the characteristic segregation energies are those of the deepest traps, as summarized in Table. VI.

Fig. 11(a) shows the inferred energy profiles across the coherent interface and along the dislocation cores (red and the black curves, respectively). By "dislocation cores" we refer to both dislocation cores and their intersections because they have almost identical segregation energies for H. Note that according to our calculations about half (-0.18 eV) of the segregation energy at the coherent interface is due to the elastic elongation of the Fe crystal. Therefore, we assumed that the energy profile first bends down smoothly to this value as it approaches the interface and then drops down directly at the interface. This does not apply to the case of dislocation cores, where the strain due to the lattice mismatch is released.

The energy profiles in the presence of C vacancies, both at the coherent interface region and in the interior of the precipitate are illustrated in Fig. 11(b). The segregation energy for H at the C vacancies at the coherent interface is equal to that for H at the dislocation cores and their intersections, but the energy profile is affected by the elastic expansion of the Fe crystal as in the case of the coherent interface. Isolated C vacancies in the interior of the TiC particle present very deep traps for H. Due to the high solution energy for H in bulk TiC these traps are not easy to populate at moderate temperatures, but it is even more difficult for H to leave them since the escape energy to bulk TiC is very high. According to our calculations, the escape of H from the center of the C vacancy to the nearest bulk interstitial site in TiC requires energy of about 1.7 eV which is the highest escape energy detected.

In the case of percolating networks of C vacancies, the energy profile, shown as dashed black curve in Fig. 11(b), was estimated from the energy barrier of an H atom mi-

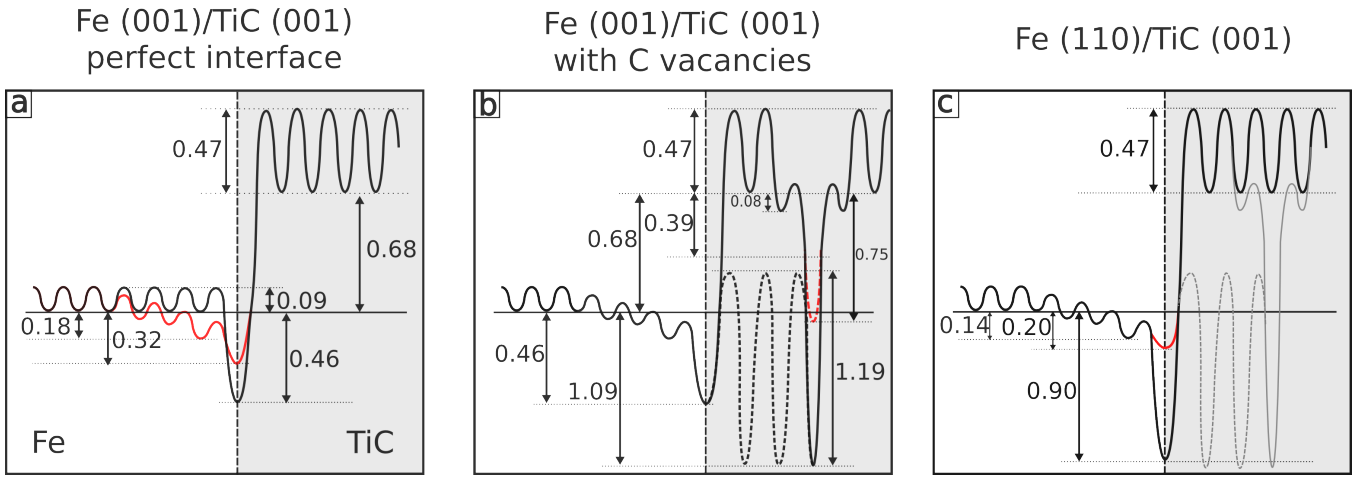

FIG. 11. (Color online) Energy profiles experienced by H atoms at: (a) the perfect coherent $(001)_{\mathrm{Fe}}/(001)_{\mathrm{TiC}}$ interface (red curve) and the misfit dislocation core therein (black curve); (b) coherent $(001)_{\mathrm{Fe}}/(001)_{\mathrm{TiC}}$ interface with single C vacancies at the interface and in the interior of the carbide (black curve), connected vacancies (dashed black curve), and single C vacancy in the interior of the carbide with double H occupancy (red dashed curve); (c) $(110)_{\mathrm{Fe}}/(001)_{\mathrm{TiC}}$ interface with (black curve) and without (red curve) C vacancies at the interface, and with C vacancies in the interior of the carbide (grey line).

grating between neighboring vacancies in bulk TiC. In this case, both the trapping depth and the barrier height for H to enter in the traps are markedly reduced in comparison to isolated vacancies. Finally, the energy profile resulting from double H occupancy of the C vacancies is shown as the dashed red line. In this case, the mutual repulsion between the two H atoms reduces strongly the trapping depth. However, it should be noted that the double occupancy is not thermodynamically stable with respect to a single-occupied vacancy and the second H residing in an interstitial position in bulk TiC.

In Fig. 11(c) the energy profiles around the $(110)_{\mathrm{Fe}}/(001)_{\mathrm{TiC}}$ interface, both perfect (red dashed curves) and with C vacancies (black full curves), are illustrated. Again, the perfect interface does not offer deep traps while the C vacancies act as strong traps. Since the presence of the interface does not influence much the TiC structure, all results regarding the trapping of H in the interior of the carbide, as presented in Fig. 11(b), are valid in this case as well.

Comparison with experiments

Using the DFT data presented in Sec. IV, we were able to construct the energy profiles (Fig. 11) for various interface configurations. To compare these results with the available experimental data it is useful to relate them with the precipitate size. Very small precipitates are cube-shaped and all their interfaces are coherent with the $(001)_{\mathrm{Fe}}/(001)_{\mathrm{TiC}}$ orientation[22]. Because of their small size, we expect them to have a negligible content of C vacancies. Therefore, the only possible trap sites are those due to the coherent interface.

As the precipitate grows, it becomes plate-shaped[22] with two large, parallel semi-coherent interfaces with the Backer-Nutting orientation relationship and a narrow lateral interface without strong preferential orientation. Only in some cases[22], the lateral interface was found to be faceted with the $(011)_{\mathrm{Fe}}/(001)_{\mathrm{TiC}}$ orientation. The C vacancies become more abundant, especially as the particle size increases, i.e., larger volume corresponds to higher probability of having carbon vacancies. From our calculations, the lateral interfaces apparently do not offer deep traps (cf. Fig. 11(c)). Moreover, since these interfaces are not very extended, they cannot contribute significantly to the trapping. Therefore, H atoms should be trapped mainly in the misfit dislocation cores on the large semi-coherent interfaces of the precipitate. This is in agreement with direct experimental observations of deuterium atoms trapped at nano-sized TiC and VC semi-coherent precipitates, performed by Takahashi et al.[23,31] using atom probe tomography.

Large TiC particles in Fe have an ellipsoidal shape with mostly incoherent interfaces[22]. The size for which the particle becomes incoherent can range from a few tens of nanometers to several micrometers, depending on the steel composition and manufacturing conditions. Direct first-principles investigations of such incoherent particles are not feasible, but some of the obtained results are valid also in this case, in particular, those for the C vacancies in the interior of the TiC particles and for the $(110)_{\mathrm{Fe}}/(001)_{\mathrm{TiC}}$ interface with C vacancies.

Most of the available experimental data were obtained using the thermal desorption spectroscopy (TDS). In these experiments, the measured quantity is the desorption activation energy, E_{des}, which does not correspond to the segregation energy but rather to the trap escape energy. Hence, for a quantitative comparison with the experimental results it is more appropriate to consider the theoretical trap escape energy, defined in Eqs. 4 and 5. Additionally, for interface configurations where the Fe

matrix is significantly expanded, it is necessary to take into account the bending of the energy profile due to the elastic expansion [see the red curve in Fig. 11(a)], which effectively leads to a local lowering of the solution energy at the interface. Our calculated ΔE_{esc} for all traps considered here are reported as function of the particle character in the left panel of Fig. 12.

In the right panel of Fig. 12, the experimental E_{des} are reported as function of the particle size. The values are obtained by studies of Wei and Tsuzaki[20–22], Escobar et al.[26], Lee and Lee[15], and Pressouyre and Bernstein[13]. In the former two studies[20–22,26], various lab processing techniques and conditions were applied in order to investigate samples with distinguishably different microstructures. In this way, it was possible to link H desorption energies to specific TiC precipitate sizes. In contrast, Lee and Lee[15] and Pressouyre and Bernstein[13] investigated samples containing precipitates with relatively large size ranges. This is indicated in Fig. 12 by the solid horizontal lines that span the range of sizes reported in these studies.

From comparison of the two panels in Fig. 12, it is obvious that some trap escape energies calculated in this work coincide very well with those reported in the considered experimental investigations. Very small particles, which are fully coherent with the matrix, have a low, constant desorption energy that can be identified with that from perfectly coherent interfaces. Precipitates larger than about 4 nm contain deeper traps which can be naturally associated with the misfit dislocation cores at the semi-coherent interfaces. In both these cases, we obtain an excellent agreement between the experimental data and the theoretical predictions, in spite of the approximations used in the calculations.

When the particle size exceeds about 10-14 nm, a broad range of desorption energies from about 0.6 to 1.8 eV have been reported in the experimental studies. Wei et al.[21,22] and Escobar et al.[26] carried out detailed analyses of the deepest traps (> 1.0 eV) and found that it is not possible to charge them with H by cathodic charging at room temperature. It was concluded that H atoms can be absorbed in these traps only at high temperature during heat treatment. Furthermore, Wei and Tsuzaki[22] were able to correlate the amount of H segregated in these traps with the volume of the precipitates but not with their surface area. Based on these findings, it is plausible to associate the largest desorption energies in Fig 12 with trapping of H atoms in C vacancies inside the TiC precipitates. However, neither the reported experimental observations nor our theoretical results allow to identify the precise nature of the trapping mechanism involved. From our results, we can only exclude the role of isolated vacancies in the interior of the carbides, since the trap escape energy seems to be too high. Since the experimental results are rather scattered, it is possible that the deep trapping is associated with a collective effect of different traps. In fact, as mentioned in the introduction, the reported experimental data are indirect measurements which need interpretations. Such interpretations can be done in different ways and involve several approximations as described in Refs.[24,28,30,69]. In this case, one of the main approximation is that once H is released from its trap, it diffuses out of the material without encountering any further barriers[20,22,26,28]. This can be a good approximation for the traps at the interface (the migration energy barrier in bulk Fe is very low), but it is more critical for the traps inside the carbides where H atoms have to penetrate through the TiC particle in order to diffuse out of the material.

Note that the work of Pressouyre and Bernstein is the only one (to our knowledge) that reports deep traps (about 0.9 eV) that could become populated at room temperature. They attributed these traps to the TiC/Fe interfaces, but they did not provide any further evidence supporting this hypothesis. According to our results, the only possible trap with such a characteristics is provided by C vacancies at the incoherent $(110)_{\mathrm{Fe}}/(001)_{\mathrm{TiC}}$ interface.

C. Influence of precipitates on the distribution of H

The calculated segregation energies for various types of traps associated with TiC precipitates enable us to estimate how these traps influence the overall H distribution and whether they effectively reduce the amount of H that can be accumulated at relevant trap sites, for instance, at dislocation cores in the Fe matrix. Since a full quantitative treatment of this problem is rather difficult and out of the scope of this study, we restrict ourselves to provide here only a semi-quantitative estimate.

Itakura et al.[70] investigated the segregation of H at screw dislocations in bcc Fe. They reported a maximum segregation energy of about -0.25 eV. Similar results have been reported by Kimizuka et al.[71]. Based on these results and our segregation energies for TiC precipitates, we can then estimate how the carbides influence the H population at cores of screw dislocations in Fe.

We considered three different concentrations ($\rho_1 = 8 \cdot 10^{-6}$ nm^{-3} , $\rho_2 = 10^{-6}$ nm^{-3}, and $\rho_3 = 3 \cdot 10^{-7}$ nm^{-3}) for disk-shaped semicoherent precipitates with a diameter of 15 nm. These values have been inferred from the experimental investigations of Wei and Tsuzaki[22] and Takahashi et al.[31]. Furthermore, we assume that the precipitates are so thin that the only possible trap sites are provided by the coherent interface regions and by the misfit dislocations cores. By employing a series of Langmuir-McLean models[34,72–74], we can first determine the occupancy of the traps at the semicoherent interfaces of the particles, and subsequently also the resulting changes of the H concentration at screw dislocations in Fe for a given concentration of TiC precipitates. Details of these calculations are given in Appendix B.

Fig. 13 shows a relative reduction of the H occupancy at dislocation cores (at T=300 K) for the three considered

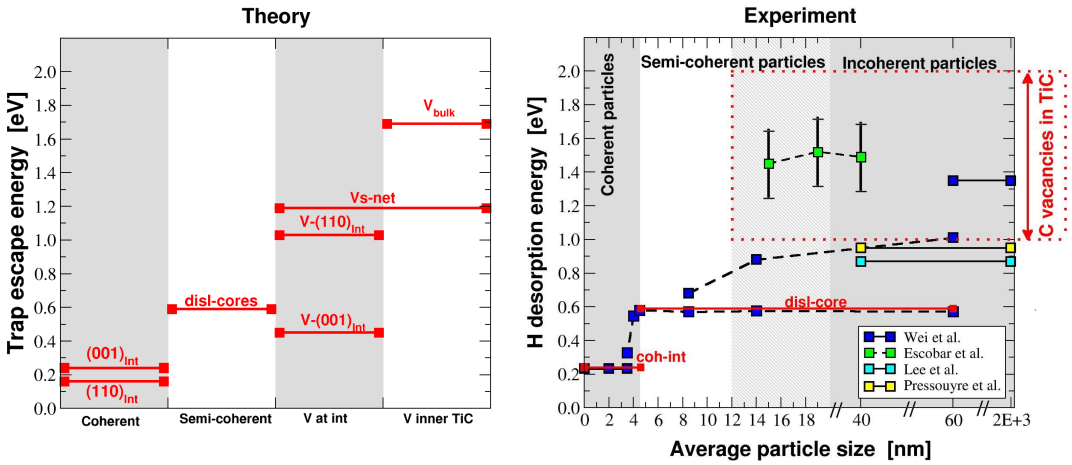

FIG. 12. (Color online) Left panel: trap escape energies (calculated according to Eqs. 4 and 5) as function of the source of traps (coherent interface, semi-coherent interface, C vacancies at the interface, and C vacancies inside the TiC precipitate). The labels refer to those in Table. VI. In addition, the escape energy from a percolating network of C vacancies is labeled as "Vs-net". Right panel: H desorption energies extracted from various experimental studies (see the text) as function of the average size of the particles. The left dark-grey region of the plot indicates the size range of coherent TiC particles, the middle white and light-grey regions indicate the size range of semi-coherent TiC particles, and the dark-grey region on the right indicates the size range of incoherent particles. Note that since Pressouyre and Bernstein carried out electrochemical permeation measurements (not TDS), the reported values are not strictly desorption energies. For comparison the most relevant trap escape energies are marked in red.

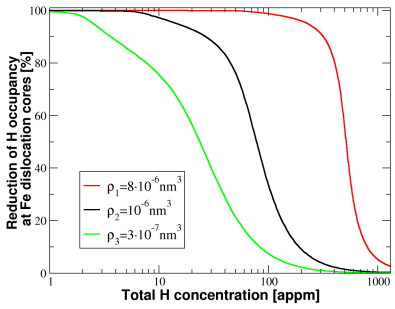

FIG. 13. (color online) Reduction of the H occupancy at Fe screw dislocation cores due to the presence of different concentrations of semi-coherent carbide precipitates at T=300 K.

TiC concentrations as function of the total H concentration. The results indicate that the effectiveness of the considered traps to reduce the amount of H which can be trapped at dislocation cores is strongly dependent on the precipitate density. For instance, at a reasonable bulk H concentration of 50 atomic ppm, the dislocation cores are essentially unoccupied for the largest precipitate density ρ_1 while for the lowest density ρ_3 the occupation is reduced by only 20%.

It is important to bear in mind that the presented results have to be considered as rough estimates only since effects due to dislocation strain fields and to the presence of other extended traps, such as grain boundaries[37] and other types of dislocations, have not been taken into account. However, it has been shown that rather shallow traps can reduce significantly the amount of H at critical sites, provided that the trap density is large enough. Therefore, it may not be necessary to have very deep traps which immobilize permanently the diffusible H atoms, as often assumed in the literature[24,25,28].

VI. CONCLUSIONS

In this work, the interaction between interstitial H and TiC precipitates in Fe has been investigated in detail. Several types of Fe/TiC interfaces and the interior of the carbide were considered as possible sources of traps for H atoms. In particular, we have acquired the energetics associated with H trapping for $(001)_{\mathrm{Fe}}/(001)_{\mathrm{TiC}}$ semicoherent interfaces, $(110)_{\mathrm{Fe}}/(001)_{\mathrm{TiC}}$ interfaces, C vacancies at these interfaces, and various C vacancy complexes in the interior of the carbides. The key findings are summarized as:

1. There is no single trapping energy associated with TiC particles, but the trapping energies depend sensitively on the trapping site and type of a trap.

2. H trapping at the semicoherent interfaces between TiC particles and Fe matrix is moderate, the trap energy ranges between −0.32 eV for coherent interface segments and −0.50 eV for misfit dislocation cores.

3. C vacancies in the interior of TiC are the strongest traps but their population can happen only at high

temperatures.

4. The energy barrier for populating C vacancies is reduced in case of carbides with percolating networks of C vacancies, but this requires rather substoichiometric carbides.

5. In the case of coherent and semicoherent interfaces, the comparison with available experimental results reveals a very good agreement and contributes to clarify the nature of the experimentally observed trapping behavior.

6. In the case of C vacancies, the spread of trapping energies is in the range of experimental results for the deepest traps, but in this case a direct quantitative comparison is not possible.

7. We estimated the reduction of the H population of cores of screw dislocations in Fe due to the presence of semicoherent precipitates. We found that the H content at dislocation cores is significantly reduced only for high concentrations of carbide precipitates.

We believe that the results obtained in this study are qualitatively valid for other types of carbide precipitates, provided that they have the same rock-salt structure. Our preliminary investigations of H interaction with other carbide precipitates seem to confirm this hypothesis.

ACKNOWLEDGMENTS

This work was supported by the European Union under the Seventh Framework Programme, grant number 263335, MultiHy (Multiscale Modeling of Hydrogen Embrittlement), and under the Research Fund for Coal and Steel (RFCS) within the project HYDRAMICROS (RFCS-CT-2010-00020). MM was partly supported by the Helmholtz Portfolio Project Energy Materials EMR. The work of RN has been performed in part under the auspices of the U.S. Department of Energy by Lawrence Livermore National Laboratory under Contract DE-AC52-07NA27344.

Appendix A

In order to avoid serious finite-size effects when calculating the H segregation energies at the $(001)_{\mathrm{Fe}}/(001)_{\mathrm{TiC}}$ interface, we performed several convergence tests using supercells with different dimensions. The lateral size has been varied in order to have a small (S), medium (M), large (L) and extra-large (XL)supercell (see the left panel of Fig. 14). In addition, for supercells with the small and extra-large lateral dimensions we varied also the number of Fe and of TiC atomic layers perpendicular to the interface, $\mathrm{N_{Fe}}$ and $\mathrm{N_{TiC}}$, respectively.

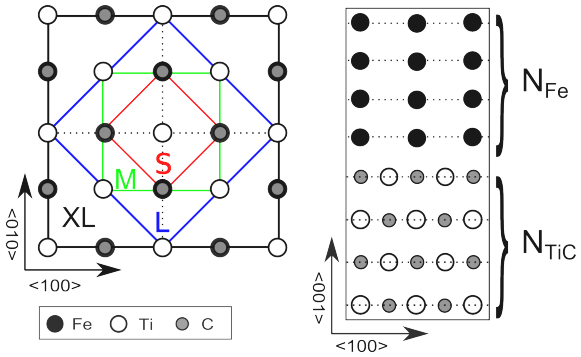

FIG. 14. Different supercell sizes used for monitoring the convergence of the segregation energies; both the lateral dimension of the supercell and the number of atomic layers perpendicular to the interface were varied.

The results of the convergence tests are reported in Table VII. They show that the small (S) cell with five layers of Fe and five layers TiC is already sufficiently large for a reliable determination of the segregation energy of H at the perfect interface. For calculations of defective interfaces (containing C vacancies), it is necessary to use supercells with at least medium (M) sized cells (see main text for details).

$\mathrm{N_{Fe}}$=5 $\mathrm{N_{TiC}}$=5			
Lateral size	$\Delta E_{\mathrm{seg}}^{FP_1^A}$	$\Delta E_{\mathrm{seg}}^{FP_2^A}$	$\Delta E_{\mathrm{seg}}^{FP_3^A}$
S	−0.32	−0.16	−0.30
M	−0.31	-	-
L	−0.32	-	-
XL	−0.31	-	-
$\mathrm{N_{Fe}}$=12 $\mathrm{N_{TiC}}$=8			
Lateral size	$\Delta E_{\mathrm{seg}}^{FP_1^A}$	$\Delta E_{\mathrm{seg}}^{FP_2^A}$	$\Delta E_{\mathrm{seg}}^{FP_3^A}$
S	−0.30	-	
XL	-	−0.17	−0.30

TABLE VII. Segregation energy $\Delta E_{\mathrm{seg}}^{i}$ for the different supercell sizes illustrated in Fig. 14.

Appendix B

The Langmuir-McLean model[34,72–74] allows to estimate the equilibrium H concentration at a defect, c_x, as function of the equilibrium H concentration in the perfect bulk crystal, c_{bulk}, at finite temperature as

$$\frac{c_x}{1-c_x} = \frac{c_{\mathrm{bulk}}}{1-c_{\mathrm{bulk}}} e^{-\Delta E_{\mathrm{seg}}/kT}, \qquad \text{(B1)}$$

where ΔE_{seg} is the segregation energy for H at the defect. With this relation we take into account the configurational entropy only, which is considered to be the most important entropy contribution[72,73].

We express the reduction of the H occupancy at screw dislocation cores due to precipitates (plotted in Fig. 13)

as

$$R(c_{\rm tot}) = \frac{c_{sd}^{\rho=0}(c_{\rm tot})}{c_{sd}^{\rho}(c_{\rm tot})} \tag{B2}$$

where $c_{sd}^{\rho=0}$ and c_{sd}^{ρ} are the H concentrations at the cores of Fe screw dislocations when there are no precipitates in the Fe matrix and with TiC precipitates of density ρ, respectively. All quantities in Eq. B2 are functions of the total H concentration in the sample, $c_{\rm tot}$.

Eq. B1 can be used to express the H concentration at the screw dislocation cores as

$$\frac{c_{sd}}{1-c_{sd}} = \frac{c_{\rm free}}{1-c_{\rm free}} e^{-\Delta E_{\rm seg}^{sd}/kT}, \tag{B3}$$

where $\Delta E_{\rm seg}^{sd}$ is the segregation energy for H at the screw dislocation core, and $c_{\rm free}$ is the concentration of free H in the system that is not trapped by the precipitates. This latter quantity can be written as

$$c_{\rm free} = c_{\rm tot} - n_{md}c_{md}(c_{\rm free}) - n_{coh}c_{coh}(c_{\rm free}), \tag{B4}$$

where c_{md}, c_{coh}, n_{md} and n_{coh} are the H concentrations and the densities of traps associated with the TiC precipitates (*md*: misfit dislocation cores, *coh*: coherent regions of the interfaces). Note that in the case of system without TiC precipitates it is $c_{\rm free} = c_{\rm tot}$.

The density of traps at the coherent interfaces, n_{coh}, was determined based on the calculations for the Fe-on-C interface configuration and multiplied by the density of precipitates (with diameter of 15 nm and two broad interfaces) in the sample, ρ. The n_{md} was estimated in analogous way, assuming that the distance between the misfit dislocation cores was 4.6 nm.

The H concentrations $c_{coh}(c_{\rm free})$ and $c_{coh}(c_{\rm free})$ were calculated using Eq. B1 with the corresponding segregation energies for H at the misfit dislocation and the coherent interface (cf. Table VI).

* distefanodav@gmail.com
† matous.mrovec@iwm.fraunhofer.de

[1] S. Lynch, J. Fail. Anal. Prev. **3**, 33 (2003).
[2] M. Loidl and O. Kolk, Adv. Mater. Processes **169**, 22 (2011).
[3] G. Lovicu *et al.*, Metall. Mater. Trans. A **43**, 4075 (2012).
[4] J. A. Ronevich, J. G. Speer, and D. K. Matlock, SAE International Journal of Materials and Manufacturing **3**, 255 (2010).
[5] J. Ronevich, S. Kim, J. Speer, and D. Matlock, Scripta Materialia **66**, 956 (2012).
[6] J. H. Ryu, Y. S. Chun, C. S. Lee, H. Bhadeshia, and D. W. Suh, Acta Materialia **60**, 4085 (2012).
[7] A. Nagao, C. D. Smith, M. Dadfarnia, P. Sofronis, and I. M. Robertson, Acta Materialia **60**, 5182 (2012).
[8] M. Koyama, C. C. Tasan, E. Akiyama, K. Tsuzaki, and D. Raabe, Acta Materialia **70**, 174 (2014).
[9] J. Rehrl, K. Mraczek, A. Pichler, and E. Werner, Materials Science and Engineering: A **590**, 360 (2014).
[10] T. Depover, D. P. Escobar, E. Wallaert, Z. Zermout, and K. Verbeken, International Journal of Hydrogen Energy **39**, 4647 (2014).
[11] A. Laureys, T. Depover, R. Petrov, and K. Verbeken, International Journal of Hydrogen Energy **40**, 16901 (2015).
[12] C. Tasan, M. Diehl, D. Yan, M. Bechtold, F. Roters, L. Schemmann, C. Zheng, N. Peranio, D. Ponge, M. Koyama, *et al.*, Annual Review of Materials Research (2015).
[13] G. M. Pressouyre and I. M. Bernstein, Metall. Trans. A **9**, 1571 (1978).
[14] G. M. Pressouyre, Acta Metall. **28**, 895 (1980).
[15] H. G. Lee and J.-Y. Lee, Acta Metall. **32**, 131 (1984).
[16] A. Turnbull, R. Ballinger, I. Hwang, M. Morra, M. Psaila-Dombrowski, and R. Gates, Metallurgical Transactions A **23**, 3231 (1992).
[17] R. Valentini, A. Solina, S. Matera, and P. De Gregorio, Metallurgical and Materials Transactions A **27**, 3773 (1996).
[18] S. Yamasaki and T. Takahashi, Tetsu-to-Hagané **83**, 454 (1997).
[19] B. Pound, Acta materialia **46**, 5733 (1998).
[20] F. G. Wei, T. Hara, and K. Tsuzaki, Metall. Mater. Trans. B **35**, 587 (2004).
[21] F. G. Wei and K. Tsuzaki, Metall. Mater. Trans. A **35**, 3155 (2004).
[22] F. G. Wei and K. Tsuzaki, Metall. Mater. Trans. A **37**, 331 (2006).
[23] J. Takahashi, K. Kawakami, and T. Tarui, Scr. Mater. **67**, 213 (2012).
[24] E. J. Song, D.-W. Suh, and H. K. D. H. Bhadeshia, Comput. Mater. Sci. **79**, 36 (2013).
[25] B. A. Szost, R. H. Vegter, and P. E. J. Rivera-Díaz-del Castillo, Metall. Mater. Trans. A **44**, 4542 (2013).
[26] D. P. Escobar, E. Wallaert, L. Duprez, A. Atrens, and K. Verbeken, Met. Mater. Int. **19**, 741 (2013).
[27] A. Nagao, M. L. Martin, M. Dadfarnia, P. Sofronis, and I. M. Robertson, Acta Materialia **74**, 244 (2014).
[28] I. Maroef, D. L. Olson, M. Eberhart, and G. R. Edwards, Int. Mater. Rev. **47**, 191 (2002).
[29] N. Winzer, O. Rott, R. Thiessen, I. Thomas, K. Mraczek, T. Höche, L. Wright, and M. Mrovec, Materials & Design **92**, 450 (2016).
[30] A. M. De Jong and J. W. Niemantsverdriet, Surf. Sci. **233**, 355 (1990).
[31] J. Takahashi, K. Kawakami, Y. Kobayashi, and T. Tarui, Scr. Mater. **63**, 261 (2010).
[32] T. Hickel, R. Nazarov, E. McEniry, G. Leyson, B. Grabowski, and J. Neugebauer, JOM **66**, 1399 (2014).
[33] D. Di Stefano, M. Mrovec, and C. Elsässer, Physical Review B **92**, 224301 (2015).
[34] R. Nazarov, T. Hickel, and J. Neugebauer, Phys. Rev. B **82**, 224104 (2010).
[35] A. T. Paxton and I. H. Katzarov, Acta Mater. **103**, 71 (2016).
[36] D. Tanguy, Y. Wang, and D. Connétable, Acta Mater. **78**, 135 (2014).
[37] D. Di Stefano, M. Mrovec, and C. Elsässer, Acta Mater. **98**, 306 (2015).
[38] Y. A. Du, L. Ismer, J. Rogal, T. Hickel, J. Neugebauer, and R. Drautz, Phys. Rev. B **84** (2011).
[39] D. H. Fors and G. Wahnström, Phys. Rev. B **82**, 195410 (2010).
[40] Å. Gustafson, Mater. Sci. Eng. A **287**, 52 (2000).
[41] E. Wallaert, T. Depover, B. Pieters, M. A. Arafin, and K. Verbeken, in *International Hydrogen Conference (IHC 2012)* (ASME Press, 2014).
[42] R. Benedek, A. Alavi, D. N. Seidman, L. H. Yang, D. A. Muller, and C. Woodward, Phys. Rev. Lett. **84**, 3362 (2000).
[43] H. Sawada, S. Taniguchi, K. Kawakami, and T. Ozaki, Modell. Simul. Mater. Sci. Eng. **21**, 045012 (2013).
[44] J. M. Albina, M. Mrovec, B. Meyer, and C. Elsässer, in *Proc. Int. Conf. MMM 2006*, edited by P. Gumbsch (Fraunhofer IRB Verlag, 2006) p. 819.
[45] A. Sutton and R. Balluffi, *Interfaces in crystalline materials*, Monographs on the physics and chemistry of materials (Clarendon Press, 1995).
[46] G. Kresse and J. Hafner, Phys. Rev. B **47**, 558 (1993).
[47] G. Kresse and J. Furthmüller, Comput. Mater. Sci. **6**, 15 (1996).
[48] G. Kresse and J. Furthmüller, Physical Reviews B **54**, 11169 (1996).
[49] J. P. Perdew, K. Burke, and M. Ernzerhof, Phys. Rev. Lett. **77**, 3865 (1996).
[50] D. Vanderbilt, Phys. Rev. B **41**, 7892 (1990).
[51] H. Kimizuka, H. Mori, and S. Ogata, Phys. Rev. B **83**, 094110 (2011).
[52] I. H. Katzarov, D. L. Pashov, and A. T. Paxton, Phys. Rev. B **88**, 054107 (2013).
[53] A. Ramasubramaniam, M. Itakura, M. Ortiz, and E. A. Carter, J. Mater. Res. **23**, 2757 (2008).
[54] D. E. Jiang and E. A. Carter, Phys. Rev. B **70**, 064102 (2004).
[55] J. Sánchez, J. Fullea, C. Andrade, and P. L. De Andres, Phys. Rev. B **78**, 014113 (2008).
[56] D. C. Sorescu, Catalysis today **105**, 44 (2005).
[57] H. Ding, X. Fan, C. Li, X. Liu, D. Jiang, and C. Wang, J. Alloys Compd. **551**, 67 (2013).
[58] D. A. Porter and K. E. Easterling, "Phase Transformation in Metals and Alloys," (Chapman & Hall, 1992) Chap. 3.
[59] H. O. Pierson, *Handbook of Refractory Carbides & Nitrides: Properties, Characteristics, Processing and Appli-*

cations (William Andrew, 1996).
[60] H. W. Hugosson, P. Korzhavyi, U. Jansson, B. Johansson, and O. Eriksson, Physical Review B **63**, 165116 (2001).
[61] P. A. Korzhavyi, L. V. Pourovskii, H. W. Hugosson, A. V. Ruban, and B. Johansson, Physical review letters **88**, 015505 (2001).
[62] L. Tsetseris and S. Pantelides, Acta Materialia **56**, 2864 (2008).
[63] W. Sun, H. Ehteshami, and P. A. Korzhavyi, Physical Review B **91**, 134111 (2015).
[64] H. Goretzki, Phys. Status Solidi B **20**, K141 (1967).
[65] K. Kawakami and T. Matsumiya, ISIJ Int. **52**, 1693 (2012).
[66] R. Benedek, D. N. Seidman, and C. Woodward, J. Phys.: Condens. Matter **14**, 2877 (2002).
[67] S. Sampath and R. Janisch, J. Phys.: Condens. Matter **25**, 355005 (2013).
[68] A. Arya and E. A. Carter, J. Chem. Phys. **118**, 8982 (2003).
[69] R. Kirchheim, Metallurgical and Materials Transactions A **47**, 672 (2016).
[70] M. Itakura, H. Kaburaki, M. Yamaguchi, and T. Okita, Acta Mater. **61**, 6857 (2013).
[71] H. Kimizuka and S. Ogata, Phys. Rev. B **84**, 024116 (2011).
[72] P. Lejček, "Grain boundary segregation in metals," (Springer, 2010) Chap. 4.
[73] X. Shen, D. Tanguy, and D. Connétable, Philos. Mag. **94**, 2247 (2014).
[74] R. Kirchheim, B. Somerday, and P. Sofronis, Acta Mater. **99**, 87 (2015).